DEVELOPMENTAL BIOLOGY

Transcriptional and epigenomic profiling identifies YAP signaling as a key regulator of intestinal epithelium maturation

Laura M. Pikkupeura[1,2]†, Raul B. Bressan[1,3]†, Jordi Guiu[1,4]†, Yun Chen[1,2], Martti Maimets[1,3], Daniela Mayer[1,3], Pawel J. Schweiger[1,3], Stine L. Hansen[1,3], Grzegorz J. Maciag[1,3], Hjalte L. Larsen[1,3], Kadi Lõhmussaar[3], Marianne Terndrup Pedersen[1], Joji M. Yap Teves[1,3], Jette Bornholdt[1,2], Vladimir Benes[5], Albin Sandelin[1,2]*, Kim B. Jensen[1,3]*

During intestinal organogenesis, equipotent epithelial progenitors mature into phenotypically distinct stem cells that are responsible for lifelong maintenance of the tissue. While the morphological changes associated with the transition are well characterized, the molecular mechanisms underpinning the maturation process are not fully understood. Here, we leverage intestinal organoid cultures to profile transcriptional, chromatin accessibility, DNA methylation, and three-dimensional (3D) chromatin conformation landscapes in fetal and adult epithelial cells. We observed prominent differences in gene expression and enhancer activity, which are accompanied by local changes in 3D organization, DNA accessibility, and methylation between the two cellular states. Using integrative analyses, we identified sustained Yes-Associated Protein (YAP) transcriptional activity as a major gatekeeper of the immature fetal state. We found the YAP-associated transcriptional network to be regulated at various levels of chromatin organization and likely to be coordinated by changes in extracellular matrix composition. Together, our work highlights the value of unbiased profiling of regulatory landscapes for the identification of key mechanisms underlying tissue maturation.

INTRODUCTION

The fetal intestine undergoes vast expansion and remodeling, leading to the formation of rudimentary villi and a continuous intervillus space during development (*1*, *2*). Following villus formation, equipotent epithelial progenitors give rise to functionally defined adult stem cells (*3*, *4*), which, following birth, become confined to the bottom of the intestinal crypts and are responsible for replenishment of the epithelium throughout life (*5*). Although the histological and morphological changes during this transition from the fetal to the adult intestine have been extensively described (*4*, *6*–*10*), how the process is orchestrated at the molecular level remains largely unexplored.

Here, we harnessed organoid cultures to investigate cell-intrinsic molecular determinants of epithelium maturation. Analogous to their in vivo counterparts, stem cells derived from the adult intestinal epithelium give rise to budding organoids that contain both crypt- and villus-like domains, partially recapitulating the morphology and cellular composition of the adult epithelium (*11*). In contrast, fetal progenitors cultured under identical conditions form intestinal cystic spheroids that are mostly composed of undifferentiated progenitors and do not spontaneously mature in vitro. However, upon transplantation into the adult intestinal niche, fetal organoids can engraft and differentiate into mature cell types (*4*, *12*, *13*), suggesting that their immature state in vitro is sustained by cell-intrinsic mechanisms.

Using this tractable model system, we use a combination of RNA expression, chromatin accessibility, DNA methylation, and three-dimensional (3D) chromatin conformation profiling techniques to define transcriptional and regulatory landscapes that define the two developmental states. We find that fetal and adult epithelial cells are transcriptionally distinct and that the activity of regulatory elements follows changes in local chromatin accessibility and DNA methylation levels, as well as changes in 3D chromatin interactions and compartmentalization. Furthermore, we identify changes in expression of extracellular matrix (ECM) components and activation of YAP1 signaling as a candidate regulatory mechanism of the fetal-to-postnatal transition. Our work supports a model in which cell-intrinsic mechanisms contribute to the specification of adult stem cells and provide a framework for further exploration of determinants of tissue maturation.

RESULTS

Fetal and adult intestinal organoids are transcriptionally distinct

Under growth-permissive conditions in vitro [namely, epidermal growth factor (EGF), Noggin, and R-spondin1 (ENR)], adult intestinal epithelial stem cells self-organize to form budding organoids, whereas progenitors derived from the fetal epithelium grow as cystic spheroids (*11*, *12*). The two in vitro systems recapitulate the cellular composition of their in vivo tissue counterparts, thereby providing a tractable platform to investigate cell-intrinsic mechanisms without the confounding influences of microenvironmental or broader

[1]BRIC - Biotech Research and Innovation Centre, University of Copenhagen, Copenhagen N DK-2200, Denmark. [2]Bioinformatics Center, Department of Biology, University of Copenhagen, Copenhagen N DK-2200, Denmark. [3]Novo Nordisk Foundation Center for Stem Cell Medicine, Faculty of Health and Medical Sciences, University of Copenhagen, Copenhagen N DK-2200, Denmark. [4]Institut d'Investigació Biomèdica de Bellvitge–IDIBELL, L'Hospitalet de Llobregat, 3a planta, Av. Granvia de l'Hospitalet 199, Hospitalet de Llobregat 08908, Spain. [5]GeneCore, EMBL, Heidelberg, Germany.
*Corresponding author. Email: kim.jensen@sund.ku.dk (K.B.J.); albin@binf.ku.dk (A. S.)
†These authors contributed equally to this work.

systemic cues. To characterize the differences between fetal progenitors and adult stem cells, we derived 3D cultures from the fetal [embryonic day E16.5] and adult proximal part of the murine small intestine, as described previously (*11*–*13*)—hereafter referred to as fetal enterospheres (FEnS) and adult organoids (aOrg), respectively (Fig. 1A). For the profiling assays, established cultures were transiently treated with medium containing CHIR99021 and nicotinamide (ENR + ChNic) to reduce the proportion of terminally differentiated cell types in aOrg cultures (Fig. 1A and fig. S1, A and B).

We subsequently profiled the genome-wide activity of transcription start sites (TSSs) in the two systems using Cap Analysis of Gene Expression (CAGE), a technique that allows simultaneous profiling of mRNA and enhancer RNA (eRNA) expression (*14*). On the basis of mRNA levels, we found that 35% of all expressed genes (11,386 genes) were differentially expressed between the two systems [false discovery rate (FDR) < 0.05 and absolute $\log_2$ fold change > 1; Fig. 1B, fig. S1C, and table S1]. Significantly up-regulated genes in adult cells included known markers of adult intestinal stem cells, e.g., *Olfm4*, *Ascl2*, *Cdx2*, *Gata4*, *Tcf4/Tcf7l2*, *Smoc2*, and *Hopx* (*15*–*20*), while fetal-specific genes included *Sox17*, *Clu*, *Trop2/Tacstd2*, *Cnx43/Gja1*, *Anxa1*, *Anxa3*, and *Anxa6* (Fig. 1B) (*13*, *21*, *22*).

Gene ontology (GO) analysis showed that the mRNAs up-regulated in FEnS were enriched in cell surface receptor signaling, locomotion, development, and adhesion pathways (Fig. 1C). As previously described (*21*), several of these overrepresented terms were linked to a set of FEnS up-regulated ECM genes. Conversely, the genes up-regulated in aOrg were mostly enriched in GO terms associated with metabolic processes (Fig. 1C). Comparison to the transcriptome of freshly isolated epithelial cells matching these developmental stages (see Materials and Methods for details) indicated substantial conservation of fetal- and adult-specific signatures in the established cultures (Fig. 1, D to F). We observed a significant correlation in gene expression between in vivo and in vitro E16.5 fetal epithelium and FEnS (Spearman $\rho = 0.44$, $P < 2.2 \times 10^{-16}$) and adult crypt cells and aOrg (Spearman $\rho = 0.52$, $P < 2.2 \times 10^{-16}$; Fig. 1D). Furthermore, the in vivo fetal- and adult-specific gene sets were significantly enriched among FEnS- and aOrg-specific genes, respectively (Fig. 1, E and F). Together, these indicate that despite identical culture conditions and morphological similarities, 3D cultures derived from fetal and adult epithelium display distinct transcriptional programs that reflect their original developmental state.

Fetal and adult states have discrete enhancer and promoter landscapes

To explore the mechanism underlying the transcriptional differences, we next set out to characterize the enhancer and promoter landscapes in FEnS and aOrg by combining the CAGE sequencing data with Assay for Transposase-Accessible Chromatin with sequencing (ATAC-seq) of chromatin accessibility. Consistent with previous observations (*23*), the combined analysis of the datasets showed that the vast majority (approximately 90%) of CAGE reads fell within ATAC-seq peaks (fig. S2A). By intersecting open chromatin ATAC peaks with active eRNA or mRNA CAGE peaks, we defined 13,064 candidate enhancers and 13,325 active gene promoters (Fig. 2A). As expected, ENCODE chromatin immunoprecipitation sequencing transcription factor (TF) peaks were enriched at the enhancer candidate regions when compared to ATAC-seq peaks without CAGE signal (fig. S2B; Fisher's exact test, $P < 2.2 \times 10^{-16}$; odds ratio, 3.15), suggesting that these are functional elements. Moreover, we found that 1700 (13%) of 11,386 genes had one or more alternative promoters (fig. S2C). Differential expression analysis of annotated promoters between FEnS and aOrg revealed that 2374 (17.8%) of 13,325 active promoters were significantly up-regulated in FEnS and 2597 (19.5%) in aOrg (FDR < 0.05 and absolute $\log_2$ fold change > 1; Fig. 2B). Similarly, in terms of eRNA expression, 3240 (23%) of the identified enhancer candidates were up-regulated in FEnS (FDR < 0.05 and absolute $\log_2$ fold change >1) and 4063 (29%) in aOrg (Fig. 2B). Since eRNA expression has been shown to correlate with enhancer activity (*24*), these observations suggest that the state-specific activity of regulatory elements underlies the vast gene-expression differences between the fetal and adult states.

State-specific enhancers are enriched in clusters

Given the observed changes in enhancer accessibility and the reported role of enhancer clusters in driving cell type–specific transcription (*25*, *26*), we next set out to assess the overall enhancer distribution in each state. Approximately 50% of the identified enhancers were identified in proximity (12.5 kb) to at least one other enhancer candidate, forming 2211 enhancer clusters (table S2). In agreement with observations that enhancers within larger clusters can be coregulated (*27*), we found that 1046 enhancer clusters show high eRNA expression correlation between associated enhancers (mean pairwise correlation >0.5; fig. S2D), which we termed internally correlated clusters. In addition, we observed that the internally correlated clusters were enriched for FEnS- and aOrg-specific enhancers when compared to uncorrelated clusters or single enhancers (Fisher's exact test, $P < 2.2 \times 10^{-16}$; odds ratio, 3.75; fig. S2E). This raises the possibility that internally correlated enhancer clusters may underpin the regulation of the distinct cell states.

Chromatin accessibility and CpG methylation changes reflect transcriptional changes at enhancers and a subset of promoters

We hypothesized that state-specific enhancer and promoter activity would reflect differences in chromatin accessibility. Enhancers and promoters differ in their 5′—C—phosphate—G—3′ (CpG) content, which affects chromatin structure. In particular, promoter nucleosome binding has been shown to correlate with CpG density, with CpG-dense regions being inherently nucleosome repelling (*28*, *29*). We observed a bimodal distribution of promoter CpG density with a smaller peak of CpG-sparse promoters with a density comparable to enhancers, which tend to be less CpG dense (Fig. 2C). On the basis of this observation, we categorized promoters as "CpG sparse" ($n = 1426$) and "CpG dense" ($n = 11,899$) and notably found that majority of CpG-sparse promoters (1067, 74.8%) are differentially expressed between the FEnS and aOrg, while only 32% of CpG-dense promoters (3904) show differential expression (Fig. 2D). Of note, changes in chromatin accessibility (ATAC signal) of CpG-sparse promoters, as well as enhancers, strongly correlated with gene expression (CAGE) changes (Spearman $\rho = 0.74$). In contrast, only weak correlation was observed at the CpG-dense promoters (Spearman $\rho = 0.28$), and high ATAC signal was observed at differentially expressed promoters in both states, irrespective of expression (Fig. 2E and fig. S2F). Specifically, 22% of FEnS-

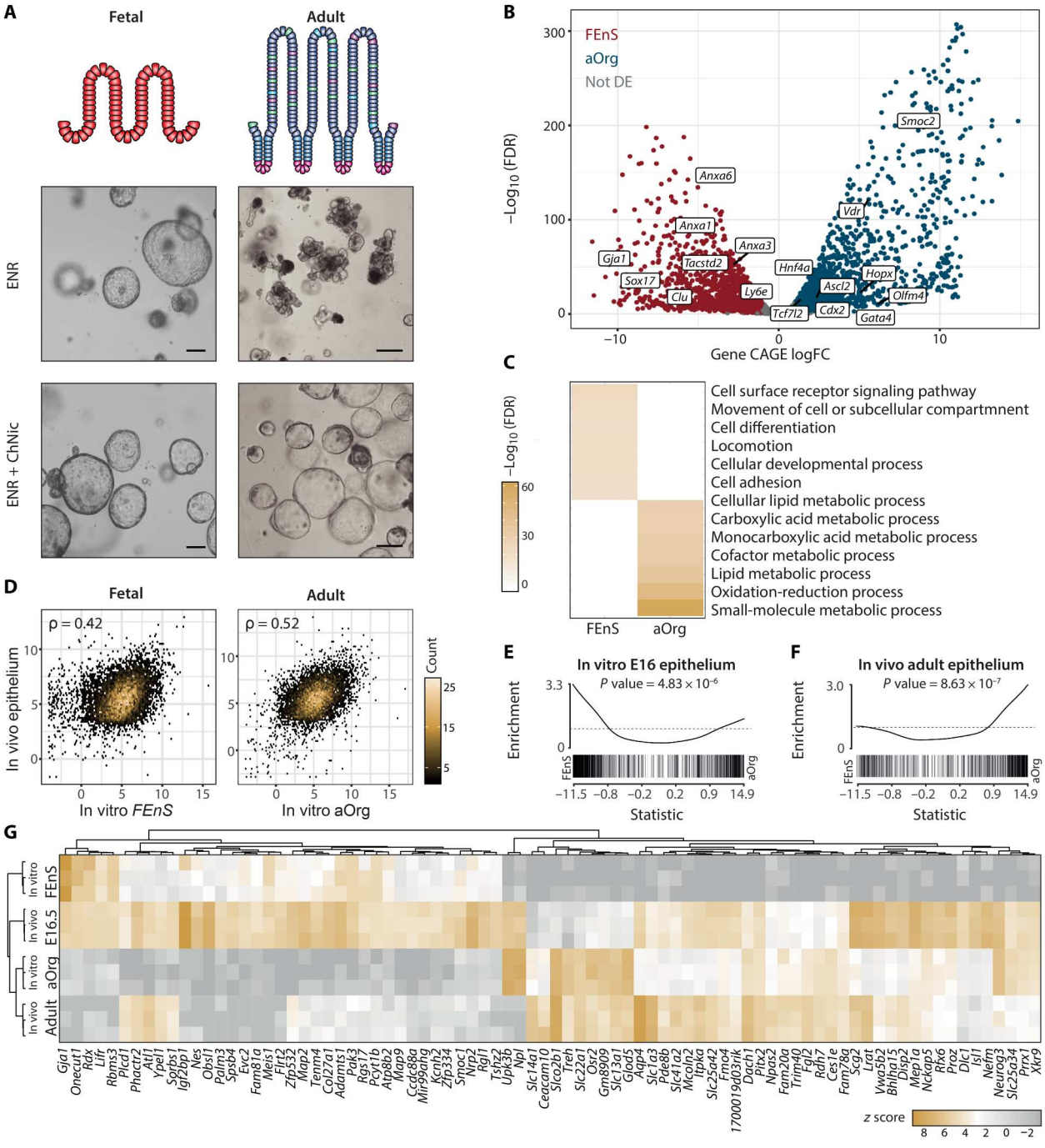

Fig. 1. Fetal and adult intestinal organoid cultures are transcriptionally distinct and recapitulate their in vivo counterparts. (**A**) Schematic representation of the fetal (E16.5) and adult small intestinal epithelium (top) and their respective in vitro derivatives (FEnS and aOrg) maintained in ENR and ENR + ChNic (bottom). Scale bars, 100 μm. (**B**) Volcano plot of CAGE differential expression analysis aggregated to the gene level of cultures maintained in ENR + ChNic. The *x* axis shows aOrg versus FEnS $\log_2$ fold changes (FC), and the *y* axis shows $\log_{10}$-transformed FDR values. Colors: red, enriched in FEnS (FDR < 0.05 and $\log_2$FC < −1); blue, enriched in aOrg (FDR < 0.05 and $\log_2$FC > 1); and gray, not differentially expressed. Previously described fetal- and adult-specific genes are labeled in the plot. (**C**) GO term enrichment analysis among genes FEnS- and aOrg-specific genes compared to all expressed genes. Color indicates the significant level of enrichment ($-\log_{10}$ FDR). (**D**) Density plots of gene expression of in vivo E16.5 epithelium versus E16.5-derived FEnS (left) and in vivo adult crypt versus in vitro aOrg (right). Spearman correlation coefficient is indicated with ρ. (**E**) Gene set enrichment analysis (GSEA) of the in vivo E16.5 genes in CAGE data sorted by aOrg versus FEnS fold change. (**F**) GSEA of the in vivo adult crypt genes in CAGE data sorted by aOrg versus FEnS fold change. (**G**) Heatmap of gene expression (top 50 most variable genes) with hierarchical clustering of in vivo E16.5 and adult epithelium and in vitro FEnS and aOrg.

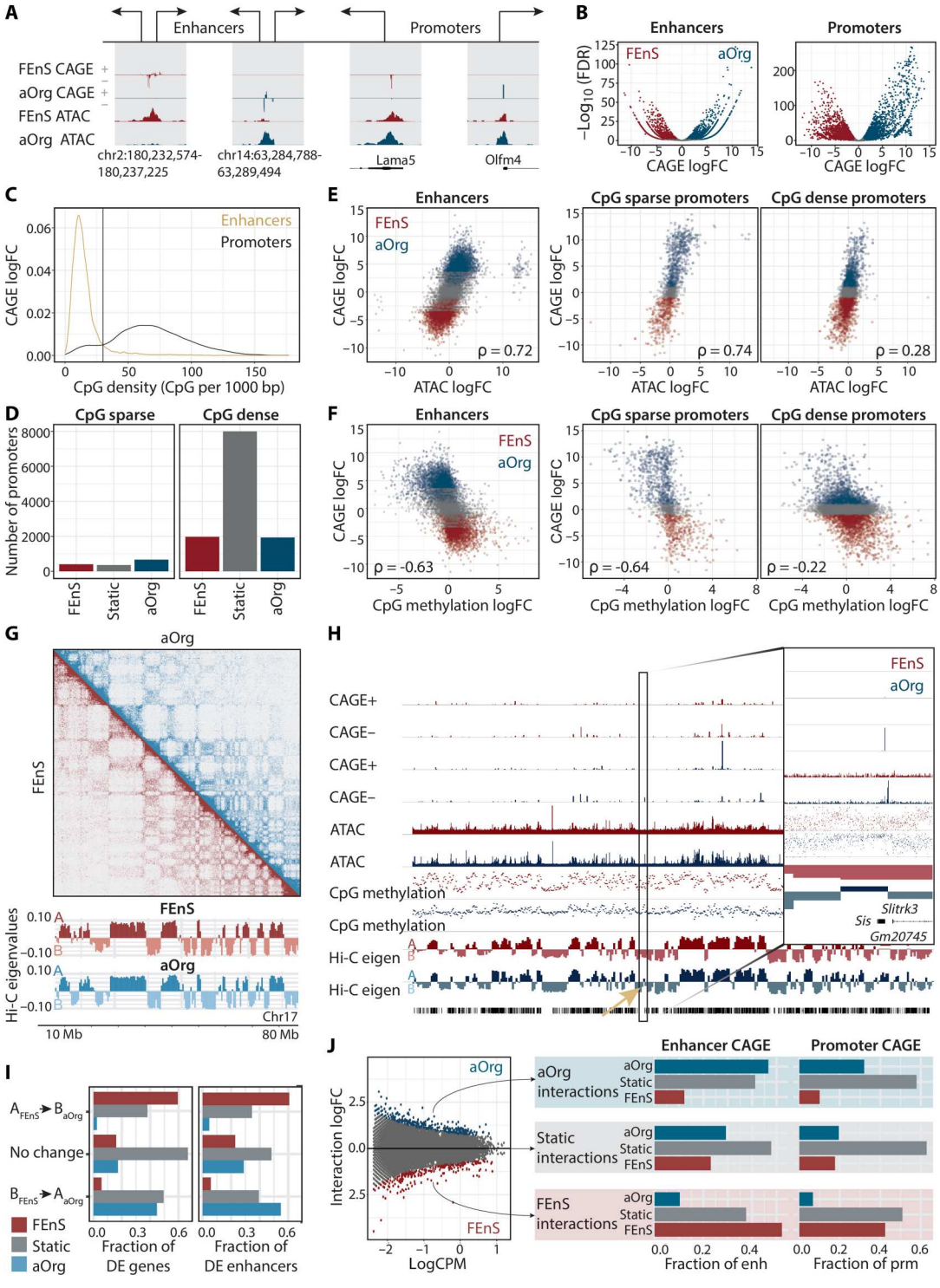

Fig. 2. Transcriptional changes reflect differences at various levels of chromatin regulation. (**A**) Schematic view of typical enhancers and promoters defined as ATAC-seq peaks with CAGE signal. (**B**) CAGE differential expression at enhancers (left) and promoters (right) with aOrg versus FEnS $\log_2$ fold changes (logFC) on the *x* axis, and $\log_{10}$-transformed FDR values on the *y* axis colored by differential expression (FEnS, red; aOrg, blue; static, gray). (**C**) Distribution of number of CpGs within 1-kb windows from enhancer center (yellow) or promoter summit (black). (**D**) Number of differentially expressed CpG-sparse (<30 CpGs per 1 kb; left) and CpG-dense promoters (right). (**E**) Correlation between ATAC logFC and CAGE logFC at enhancers and CpG-sparse and -dense promoters colored by differential expression. ρ = Spearman's correlation coefficient. (**F**) Correlation between CpG methylation logFC and CAGE logFC as in (E). (**G**) Top, representative Hi-C interaction heatmap with chr17 coordinates as axis. Bottom, eigenvalues of the first principal component (PC1) of 500-kb bins along chromosome 17 for each state colored by state (FEnS, red and aOrg, blue) and compartment (A, dark and B, light). Both plots represent averages of two biological replicates. (**H**) CAGE signal from + and − strand, ATAC, CpG methylation, eigenvalues of Hi-C PC1, and RefSeq annotation along chr3. Zoom-in contains $B_{FEnS} \geq A_{aOrg}$ transitioning region indicated by a yellow arrow. (**I**) Faction of differentially expressed genes and enhancers within bins constitutively in A or B compartment, or $A_{FEnS} \geq B_{aOrg}$ or $B_{FEnS} \geq A_{aOrg}$ compartment. (**J**) Right, differential interactions between 100-kb bins with mean interaction counts per million (CPMs) on the *x* axis and interaction logFC on the *y* axis, colored by differential interactions (aOrg, blue; FEnS, red; static, gray). Left, fraction of differentially expressed enhancers and promoters overlapping the differentially interacting bins on the *x* axis and differential expression of the enhancers and promoters on the *y* axis, split by direction of differential interactions.

and 29% of adult-specific enhancers exhibited differences in the levels of activation in the respective state (FDR < 0.05 and absolute $\log_2$ fold change >1). Similarly, 22% of FEnS- and 29% aOrg-specific CpG-sparse promoters were differentially accessible, while this was only the case for 8% of FEnS- and 8% of aOrg-specific CpG-rich promoters. We, thus, conclude that chromatin accessibility at enhancer regions and a subset of promoters with low CpG density is dynamically regulated across developmental states and co-occurs with expression changes. In contrast, most promoters are constitutively accessible despite prominent transcriptional changes.

Given the correlation between dynamic chromatin accessibility and promoter GC content, we next hypothesized that enhancer and promoter activity at these GC-sparse regions would correlate with DNA methylation levels. Changes in DNA methylation between intestinal fetal progenitor and adult stem cells have been reported in vivo (*30*). We, therefore, analyzed differences in CpG cytosine methylation between FEnS and aOrg cultures using whole-genome bisulfite sequencing (WGBS). We observed a strong negative correlation between expression and methylation at enhancers (Spearman $\rho = -0.63$) and CpG-sparse promoters (Spearman $\rho = -0.64$) but only a weak negative correlation at CpG-rich promoters (Spearman $\rho = -0.22$), which were constitutively hypomethylated (Fig. 2F and fig. S2G). Analysis of differentially methylated regions (DMRs) revealed that 155 (38.5%) CpG-sparse aOrg-specific promoters were hypomethylated in aOrg, and 288 (43.3%) of the FEnS-specific promoters were hypomethylated in FEnS. In contrast, only 346 and 264 (17.5 and 13.7%) FEnS- and aOrg-specific CpG-dense promoters were hypomethylated in fetal and adult state, respectively. In conclusion, we found that chromatin accessibility and DNA methylation changes that are associated with eRNA expression status define each developmental stage. In contrast, only a few promoters show state-specific chromatin changes, with a vast majority of them being constitutively accessible and hypomethylated despite their expression status. Together, these suggest that developmental programs are regulated by differential enhancer usage rather than local promoter accessibility changes.

Large-scale chromatin structure is broadly conserved in fetal and adult organoids

Since the gene expression programs appeared to be mostly regulated by distal elements, we next inquired whether changes in the 3D chromatin structure would be an important determinant of state-specific transcription. Given the evidence for the role of the genome compartmentalization into active (A) and inactive (B) chromatin compartments in cell fate transitions (*31*–*34*), we first combined in situ deoxyribonuclease (DNase) Hi-C with DNA methylation profiling to investigate these large-scale chromatin changes. Using an eigenvector-based approach on 500-kb genomic bins, we defined A and B compartments and observed that the overall chromatin architecture was largely maintained between the two states (Fig. 2G). The Hi-C eigenvalues were negatively correlated with published data of interactions between chromatin and nuclear lamina (*35*), with negative eigenvalues (B compartment) corresponding to regions with strong lamina interactions (fig. S2H). This is consistent with the notion that nuclear lamina interactions are key to the spatial organization of chromatin, wherein B compartment regions associate closely with lamina-associated domains (LADs) and that most LADs are constitutively associated with the nuclear lamina regardless of cell type (*35*).

We noted that, although the overall chromatin structure was largely unchanged (Fig. 2G), some regions did switch compartments between fetal and adult cells. Specifically, 73 regions moved from active to inactive compartment (A FEnS → B aOrg), and 81 regions showed the reciprocal pattern (B FEnS → A aOrg), while the remaining 4787 bins remained static (either A or B in both FEnS and aOrg) (fig. S2I). Of note, by overlaying the Hi-C data with the ATAC, WGBS, and CAGE expression datasets, we observed that these few large compartment transitions were accompanied by changes in CpG methylation levels and transcriptional activity (Fig. 2H). By and large, CpG methylation levels were higher in the A compartment than in the B compartment, and compartment transitions coincided with corresponding changes in methylation levels (fig. S2J). Consistent with previous observations (*34*, *36*), we noticed that broad regions with low levels of methylation and disordered methylation patterns preferentially overlapped with the B compartment (fig. S2, K and L), thus confirming our Hi-C–based compartment annotation.

Last, we explored whether these relatively few chromatin compartmentalization changes also correlated with activation of state-specific enhancer landscapes and gene regulatory networks. We found that A FEnS → B aOrg transitioning regions were enriched for FEnS up-regulated genes and enhancer candidates, whereas aOrg up-regulated genes and enhancer candidates were enriched in B FEnS → A aOrg regions (Fig. 2I).

Transcriptional differences correlate with state-specific changes in chromatin interactions

Despite the few compartmental changes, differential interaction analysis at smaller scale (100-kb resolution) identified 3226 regions with significantly different interaction intensities in FEnS and aOrg (FDR < 0.05), which directly correlated with promoter and enhancer expression changes between the two states (Fig. 2J). Together, this indicates that despite conservation of the large-scale chromatin structure, smaller-scale chromatin reorganization correlates with transcriptional activity driven by specific regulatory elements in the fetal and adult states.

To further interrogate these finer-scale changes in chromatin organization, we next defined chromatin domain boundaries that changed either strength or direction between the two states (n = 3113) (fig. S2, M and N). As previously described, these are likely to correspond to changes in organization of self-interacting topologically associated domains (*37*). Intriguingly, enhancers that occurred in clusters were generally in closer proximity (<50 kb) to these changing chromatin boundaries when compared to single enhancers (Fisher′s exact test, $P = 6.9 \times 10^{-7}$; odds ratio, 1.26). In addition, we found that differentially expressed genes were enriched in regions adjacent (<50 kb) to changing chromatin boundaries (Fisher′s exact test, $P = 1.1 \times 10^{-5}$; odds ratio, 1.22; table S3). Collectively, these analyses demonstrate that local chromatin rearrangements might underlie state-specific differential enhancer and transcription activity between fetal and adult cells.

Different TFs are associated with stage-specific chromatin changes

Given the well-established role of lineage-specific TFs as major determinants for cellular identity, we reasoned that differences in gene expression were likely associated with activity of stage-specific TFs. We found that 159 and 144 TFs were significantly up-regulated in

FEnS and aOrg, respectively (FDR < 0.05 and absolute $\log_2$ fold change >1; Fig. 3A). These included TFs previously described to play roles in cellular identity in the fetal and adult intestine, such as SOX17 and GATA4, respectively (Fig. 3A and fig. S3, A and B) (*19*, *22*). Predicted binding sites for these differentially expressed TF were enriched in stage-specific enhancers and promoters. For instance, FEnS promoters and enhancers were enriched for motifs associated with activating protein 1 (AP1), Transcriptional Enhanced Associate Domain (TEAD), SRY-related HMG box (SOX), and nuclear factor kappa B (NFKB) TF families, while aOrg enhancers and promoters showed enrichment for HNF4A, PPARG, CDX2, and GATA4 binding sites (Fig. 3B). Furthermore, the observed TF binding site (TFBS) enrichment was more prominent at enhancers than at promoters, in agreement with the idea that TFs predominantly exert their role at enhancer regions (*26*).

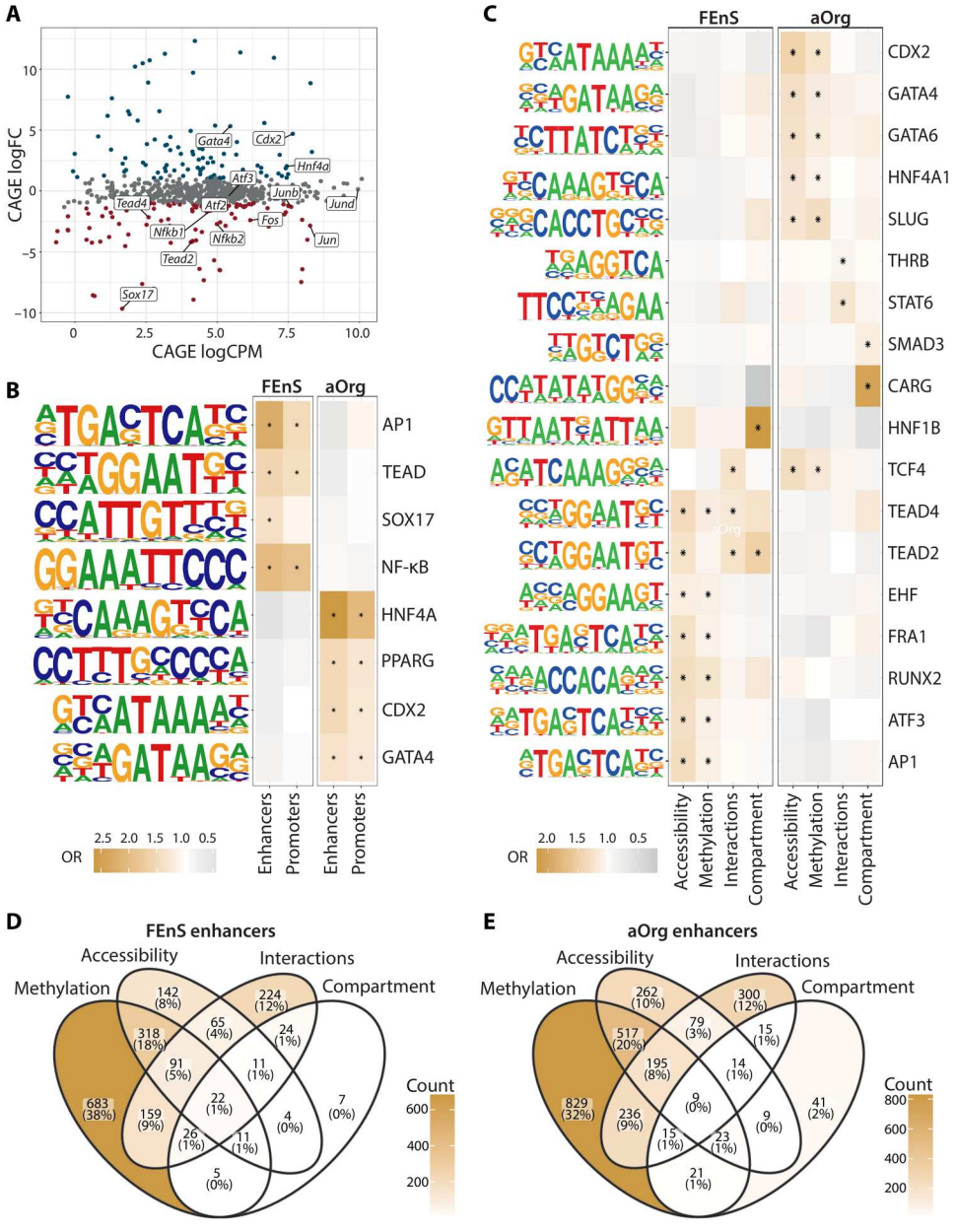

Fig. 3. Distinct TF networks drive fetal and adult state–specific promoter and enhancer activity. (**A**) MA plot of TF gene level aggregated CAGE expression $\log_2$ CPMs over $\log_2$ fold changes (FC). The TFs with motifs enrichment [as in (B)] in FEnS- or aOrg-specific promoters and enhancers [as in (B)] are labeled in red and blue, respectively. (**B**) Transcription factor binding site (TFBS) enrichment at enhancers and promoters. Each row represents one TF or a group of TFs sharing a binding motif. Color represents enrichment odds ratios (ORs) over all expressed enhancers and promoters, respectively. Enrichment with FDR value <0.05 are marked by asterisks (*). (**C**) TFBS enrichment at differentially methylated, accessible, interacting, or compartment switching enhancers compared to all state-specific enhancers. Color represents enrichment odds ratios over all expressed enhancers and promoters, respectively. Enrichment with FDR value <0.05 are marked by asterisks (*). (**D** and **E**) Venn diagrams depicting overlap of differential methylation (WGBS), accessibility (ATAC), interactions (Hi-C), and compartment status (Hi-C) among FEnS (D) and aOrg (E) specific enhancers.

Using TFBS enrichment, we next found that different TFBSs were enriched at enhancers that were either differentially methylated (WGBS) or accessible (ATAC). Stage-specific enhancers showing 3D chromatin interactions and compartment localization also showed enrichment for specific TF classes, although these differ from those enriched in the differentially methylated and accessible regions (Fig. 3C). This observation is consistent with the observation that changes in accessibility most often co-occur with changes in methylation but less frequently with changes in interactions or compartmentalization (Fig. 3, D and E).

Regardless of the mode of regulation, FEnS- and aOrg-specific enhancers showed enrichment for different classes of TFBSs (Fig. 3C). Of note, specific classes of TFBSs were enriched at enhancers with differential methylation and accessibility status and at enhancers with differential 3D interaction and compartment localization (Fig. 3C). An exception to this was TEAD (TEAD2 and TEAD4) motifs, which were consistently enriched at the FEnS-specific enhancer that showed locally accessible and methylated changes, as well as enhancers showing differential chromatin interactions and compartment activation (i.e., A FEnS → B aOrg or B FEnS → A aOrg regions) (Fig. 3C). Together, these analyses indicate that fetal progenitors and adult stem cells are regulated by different gene regulatory networks that activate divergent enhancer landscapes and that TEAD-mediated transcriptional activity might act as a major determinant of the fetal-specific transcriptional program.

Fetal progenitors are maintained by sustainably high YAP activity levels

Given the consistent occurrence of predicted binding sites for TEAD and/or AP1 factors—known coeffectors of YAP signaling (*38*)—in local and large-scale chromatin changes, we hypothesized that YAP transcriptional activity might be involved in the maintenance of the fetal progenitor state. In agreement, we found that the FEnS-specific transcriptome was highly enriched for transcriptional signatures associated with activation of YAP in intestinal epithelial cells (Fig. 4A) (*21*, *39*) and expressed high levels of the direct YAP target genes *Ankrd1*, *Ctgf*, *Cyr61*, *Clu*, and *Tnfrsf12a* (Fig. 4B). In addition, image analysis confirmed high levels of nuclear (active) YAP in FEnS compared to aOrg, in which nuclear YAP signal was restricted to fewer cells in the bud domains (Fig. 4, C and D). Of note, the YAP-associated transcriptional signature was enriched in the fetal (E16.5) epithelium compared to adult crypt cells in vivo (fig. S4, A and B). Furthermore, akin to the in vitro cultures, nuclear YAP signal was also observed throughout the E16.5 epithelium but only locally at the lower part of adult crypts in vivo (fig. S4, C and D). Together, this indicates that high YAP activity defines the fetal epithelium both in vitro and in vivo.

To functionally test the requirement for YAP activity, we next treated fetal- and adult-derived cultures with verteporfin, a commonly used inhibitor of YAP-TEAD interaction and mediated transcription (*40*). Using replating assays, we indeed observed that the growth of FEnS is more strongly affected by the inhibitor, indicating that fetal cells are more dependent on YAP activity than adult cells (Fig. 4, E and F). To rule out potential off-targets of verteporfin, we also tested two independent, highly selective TEAD inhibitors —MGH-CP1 and TED-347 (*41*, *42*)—and consistently observed a selective effect on the replating efficiency of fetal cells (Fig. 4, E and F). Last, in agreement with the described role of YAP in tissue repair, we also observed increased sensitivity to those inhibitors during early phases of aOrg cultures (from both freshly isolated crypts or recultured crypt domains following organoid splitting; fig. S4E), a process that is reminiscent of in vivo epithelial regeneration and dependent on YAP signaling (*43*, *44*).

To test whether high YAP activity was sufficient to induce conversion into the fetal state, we next derived adult cultures from an inducible TetON-hYAP/H2B-mCherry mouse strain (see Materials and Methods), in which addition of doxycycline (DOX) induced expression of a constitutively active (S127A mutant) YAP transgene. Using this system, we found that induction of YAP upon splitting caused aOrg to grow as cystic, fetal-like round structures expressing high levels of the fetal-specific cell surface marker SCA1 (Fig. 5, A and B) (*21*). Transcriptionally, YAP overexpression led to the down-regulation of various adult stem cell and differentiation markers as well as a global up-regulation of the fetal-specific gene signature (Fig. 5, C to E). However, despite morphological and transcriptional similarities to FEnS (Fig. 5, D and E, and fig. S5A), aOrg could not be maintained long-term in DOX-containing ENR medium, indicating that YAP activation alone is not sufficient to drive full conversion into a self-sustained fetal state.

To investigate how the activated YAP aOrgs differ from the fetal cells, we next compared genes differentially expressed between untreated and DOX-treated aOrg to those differentially expressed between FEnS and aOrg (−DOX). We found that 850 of the 2342 FEnS-specific genes (approximately 36%) were up-regulated in aOrg upon DOX induction (Fig. 5F and table S4). As expected, TF motif analysis at promoters of these overlapping up-regulated genes identified enrichment for TEAD and AP1 complex factors (FRA1, FRA2, and FOSL) (fig. S5B). In contrast, nonoverlapping FEnS-specific genes were enriched in RFX/X-box and E2F motifs, together indicating that other TF networks operate in conjunction with activated YAP to drive the fetal state. In agreement, GO term analyses of the 850 shared up-regulated genes (versus all expressed genes in the dataset) found specific enrichment for Hippo signaling and ECM-related pathways (fig. S5C). Digestion, absorption, and metabolic pathways remained highly enriched in aOrg, regardless of YAP activation status (i.e., both in −DOX and +DOX aOrg), suggesting that YAP overexpression can induce a fetal-like state without fully suppressing differentiation and metabolic gene networks that are operational in adult cells.

Last, using single-cell RNA sequencing (RNA-seq) profiling of fetal and adult organoids, we found that a small fraction of the cells in the fetal cultures in standard ENR medium spontaneously mature into adult-like cells (clusters 11 and 12; Fig. 5G, and fig. S6, A to D) (*45*). These "maturing" cell clusters are globally characterized by down-regulation of FEnS-specific signature with a concomitant up-regulation of aOrg signature (fig. S6, B and C). Of note, while cluster 11 showed increased expression of various adult stem cell genes, cluster 12 appeared to mature specifically into Tuft-like cells (fig. S6, D and E). While YAP-associated genes were highly expressed in most fetal cells, the maturing cell clusters also showed a much lower enrichment in the signature, suggesting that the maturation process entails a reduction in YAP activity (Fig. 5, H and h). Further corroborating this, we observed a slight increase in number of cells expressing CD117 (a cluster 12–specific cell surface specific marker) in FEnS treated with a short, sublethal dose of the YAP-TEAD inhibitors MGH-CP1 and TED-347 (fig. S6F).

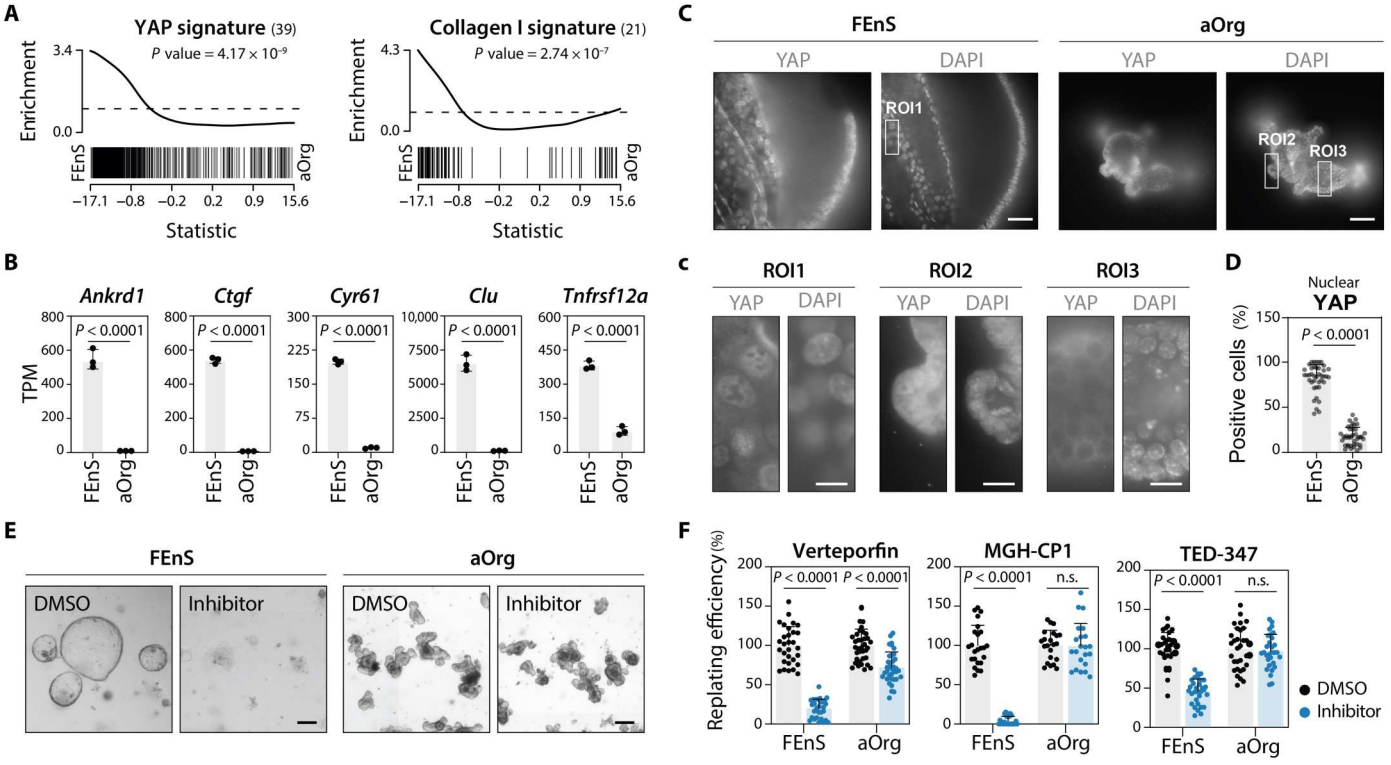

Fig. 4. Fetal cells are maintained by sustainably high levels of YAP activity. (**A**) GSEA showing enrichment of active YAP-associated gene signatures and (**B**) bar plots depicting mRNA expression levels of direct YAP target genes in FEnS and aOrg cultures (ENR medium). *P* values calculated by unpaired *t* test are shown. (**C**) Immunofluorescent analysis showing YAP subcellular localization in FEnS and aOrg grown in ENR medium. Nuclear signal is observed in most fetal cells, while adult cells show mostly cytoplasmic localization. Scale bar, 100 μm. (**c**) Higher magnification of regions of interest (ROI) highlighted in (C). Scale bar, 25 μm. (**D**) Bar plotting showing percentage of cells with high YAP nuclear signal. Each dot represents an individual FEnS or aOrg structure. *P* value defined by unpaired *t* test is shown. (**E**) Representative phase contrast images of FEnS and aOrg cultures treated with YAP signaling inhibitors. Images from MGH-CP1 treatments are shown. Scale bar, 200 μm. (**F**) Bar plots depicting replating efficiency following treatment with the indicated inhibitors. Each dot represents a technical replica of at least three independent experiments. n.s., not significant.

Differential YAP activity levels correlate to differential expression of ECM genes

Given the role of YAP as a mechanoresponsive factor (*38*), we speculated that differential expression of ECM components might underlie its differential activation levels in fetal and adult cells. In agreement, we found fetal-specific genes to be highly enriched in genes associated with cell adhesion and cell surface receptors (Fig. 1C). Similarly, ECM-related GO terms were also enriched among genes regulated at different levels (fig. S3C). Among these genes, various laminin subunits, collagens, and fibronectin were expressed at much higher levels in the fetal cells, both in vitro and in vivo (Fig. 6, A and B). This made us speculate whether fetal and adult cells would exhibit differences in the requirements for signaling downstream of integrin activation. Here, various ECM components have been shown to trigger YAP activation through integrin-mediated activation of focal adhesion kinase (FAK) and SRC family kinases (*38*); we finally tested the effects of pharmacological pathway inhibitors in culture. Consistent with the previous results using YAP inhibitors, fetal cultures showed increased sensitivity to FAK and SRC inhibitors compared to aOrg (Fig. 6, C and D), thus confirming the requirement of active YAP and the upstream signaling pathways for maintenance of the fetal cells.

DISCUSSION

Cellular state transitions such as the maturation of fetal progenitors into the adult tissue stem cells require activation of specific transcriptional programs. In the intestinal epithelium, recent works indicate that the maturation process is associated with enhancer decommissioning, changes in chromatin accessibility, and differential requirements for mitochondrial activity (*46*–*49*). Here, we used organoid cultures to further provide a comprehensive characterization of transcriptional and chromatin landscapes of fetal progenitors and adult stem cells of the intestinal epithelium. Our analyses indicate that despite few changes in chromatin compartment and promoter accessibility, widespread differences in gene expression and enhancer usage characterize each developmental stage. Together with TF motif analyses, these observations suggest that maturation is vastly regulated by differential enhancer landscapes and associated TF networks.

Integrative analyses of the state-specific regulatory elements and chromatin features identified TEAD and AP1 proteins—transcriptional cofactors of YAP signaling—as potential regulators of the fetal transcriptional program. Given the well-described role of YAP signaling in fetal development and tissue repair (*21*, *43*, *50*), we hypothesized that sustained YAP activity is a key player in the maintenance of the fetal state. We showed that fetal cells are more dependent on YAP activity and to upstream activating signals

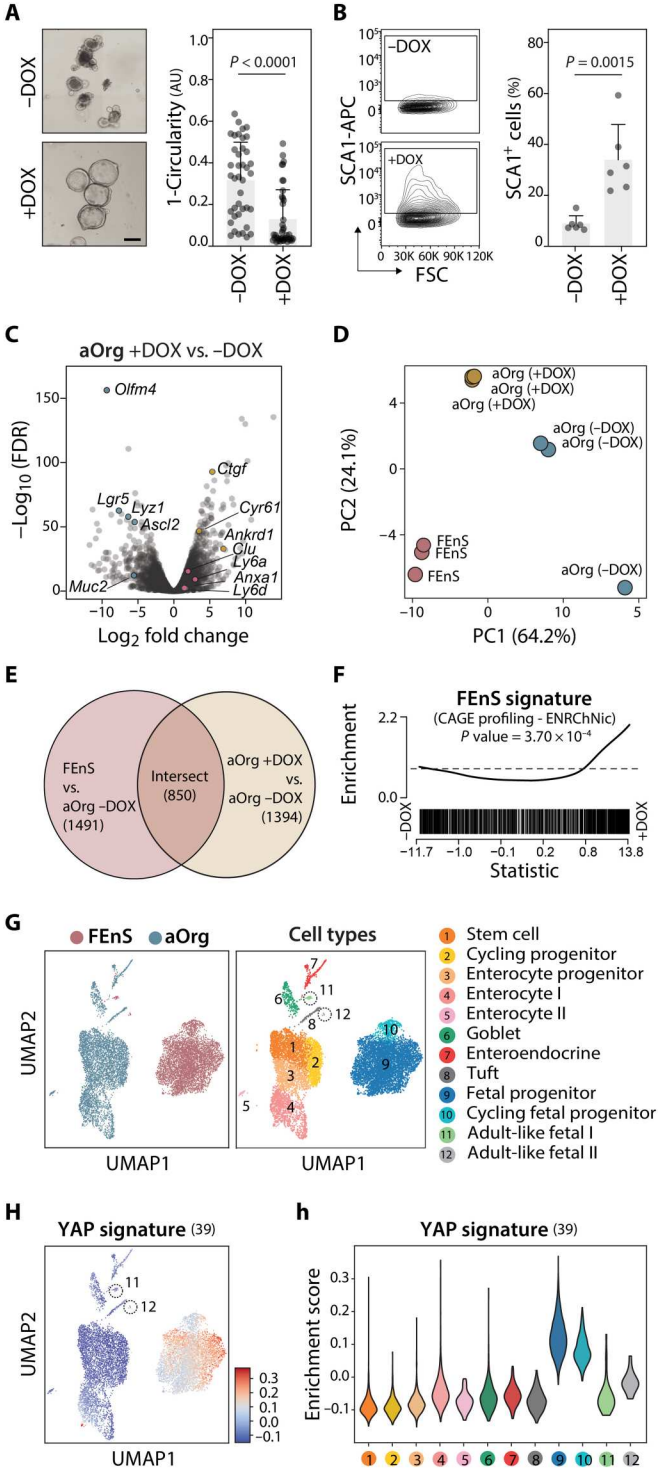

Fig. 5. Activation of YAP induces fetal-like features in aOrg cultures. (**A**) Left, representative images of TetON-YAP aOrg cultures in ENR medium with the absence or presence of DOX (±DOX). Right, bar plot depicting quantification of organoid circularity. Scale bar, 200 μm. (**B**) Analysis of SCA1 protein expression by flow cytometry in tetON-YAP aOrg cultures. (**C**) Volcano plot showing differentially expressed genes upon DOX treatment. Representative adult- and fetal-specific genes are highlighted in blue and red, respectively. Representative known YAP target genes are highlighted in yellow. (**D**) Principal components analysis (PCA) from RNA-seq profiling data from FEnS and TetON-YAP aOrg (±DOX) cultures in ENR medium. PCA was carried out on the basis of the top 1% most variable genes (i.e., 137) across all samples. (**E**) Venn plot depicting fraction of shared up-regulated genes in FEnS (versus aOrg −DOX) and aOrg +DOX (versus aOrg −DOX) cultures. (**F**) GSEA showing enrichment of FEnS-associated gene signature upon YAP induction (+DOX). (**G**) Uniform Manifold Approximation and Projection (UMAP) visualization of single cells from FEnS and aOrg cultures colored by sample (left) or cell type (right). Cell-type clusters were annotated on the basis of expression of known marker genes. (**H**) Average expression of YAP-associated gene signature overlaid on the UMAP cell-type plot. (**h**) Violin plot depicting enrichment of the YAP signature in each cell type cluster. See Materials and Methods and associated manuscript for further details on the single-cell RNA analyses in (G) and (H).

mediated by FAK and SRC, as indicated with the inhibitor experiments. In line with the elevated expression of ECM proteins, we speculate that the deposition of such components by fetal progenitors represents a cell-intrinsic mechanism to sustain YAP activity and, ultimately, reinforce the progenitor state and/or prevent their premature transition into functionally restricted adult intestinal stem cells.

Our functional and transcriptomic analyses indicate that activated YAP signaling is not the sole determinant of the fetal program, and additional pathways are likely to play key roles in safeguarding the fetal progenitor state and/or driving maturation into adult, functionally specified cells. In agreement, we found that the members of SWItch/Sucrose Non-Fermentable (SWI/SNF) chromatin remodeling complex Smarca4 and Smarcc1 also play a role

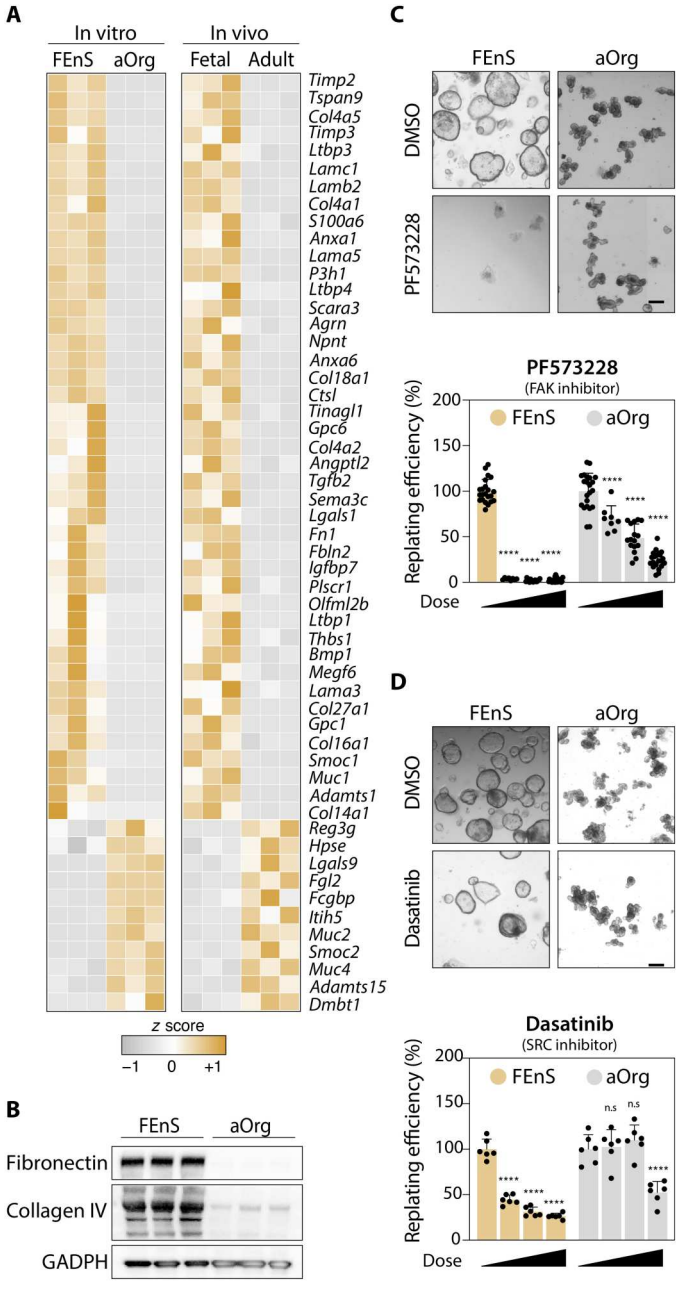

Fig. 6. FEnS and aOrg express different ECM genes. (**A**) Heatmap depiction of mRNA expression levels of ECM genes (GO: 0031012 - ECM) that are differentially expressed consistently between FEnS and aOrg and freshly isolated fetal and adult epithelial cells. (**B**) Western blot analysis of ECM proteins fibronectin and collagen IV in FEnS and aOrg ($n = 3$ independent passages each). Blot against glyceraldehyde-3-phosphate dehydrogenase (GAPDH) was used as loading control. (**C** and **D**) Replating assay of FEnS and aOrg cultures treated with the pharmacological inhibitors of FAK (C) and SRC (D) kinases. Each dot represents a technical replica of at least three independent experiments. ****$P > 0.0001$ by two-way ANOVA following multicomparison (each dose versus 0 μM for FEnS or aOrg). Scale bar, 200 μm.

in preventing precocious differentiation during intestinal epithelium development (*45*). Whether YAP and SWI/SNF complexes act in conjunction, or regulate independent axes of the fetal network, remains to be elucidated. In vivo, nonetheless, we speculate that such cell-intrinsic mechanisms operate in synergy with changes in the stroma and niche formation during morphogenesis (*1*, *5*) to ensure proper timing of intestinal stem cell maturation. Experimentally, the identification of such cell-intrinsic mechanisms might also assist the development of more robust embryonic stem cell/induced pluripotent stem cell differentiation in vitro protocols, which often result in the generation of immature cell types that are ill-suited for functional studies or cell-replacement therapies (*51*, *52*).

In summary, we demonstrate that fetal and adult intestinal progenitor/stem cells are maintained by distinct gene regulatory networks, mostly operating on the enhancer landscape. We propose that such networks constitute a key mechanism to ensure the successful maturation and/or differentiation timing of the epithelium during development. Similar mechanisms are likely to operate in the context of tissue repair and cancer, given the emerging evidence that these processes often require reacquisition of developmental transcriptional programs (*21*, *39*, *53*, *54*). We and others have previously found that regeneration of the adult intestinal epithelium entails a reprogramming process into a fetal-like state that is mediated by YAP signaling (*21*, *55*, *56*). Likewise, changes in ECM composition analogous to the fetal epithelium appear to render adult progenitor cells refractory to differentiation cues during neoplastic transformation (*57*, *58*). We, thus, envisage that the comprehensive datasets presented here will provide a framework for investigation of further determinants of epithelial maturation and help shed light on conserved mechanisms of tissue maturation, repair, and neoplasia.

MATERIALS AND METHODS

Mice

C57BL/6J mice (Taconic) were used for all the experiments unless otherwise specified. Transgenic TetON-hYAP/H2B-mCherry was generated through breeding of a Tet-YAP strain (*59*) with a Tet-H2B-mCherry strain (the Jackson Laboratory, no. 014602). None of the animals had been subjected to prior procedures. All animals were housed in specific pathogen–free animal facilities under a 12-hour light-dark cycle always with companion mice. Food and water were provided ad libitum. The Danish Animal Inspectorate has approved all animal procedures.

Adult and fetal epithelium–derived organoid cultures

Organoids were grown as previously described (*12*, *21*). Briefly, epithelial fragments from fetal intestine (intestines from three fetuses were pooled for each sample) and scraped adult crypts (from one individual per sample) were harvested from the proximal parts of the small intestine using EDTA (2 mM). Harvested epithelial fragment adult crypts were embedded in Matrigel droplets and cultured in advanced Dulbecco's modified Eagle's medium/F12 with GlutaMAX and penicillin-streptomycin supplemented with EGF (PeproTech, 50 ng/ml), Noggin (PeproTech, 100 ng/ml), and R-spondin1 (R&D Systems, 500 ng/ml). For the transcriptomic and chromatin profiling experiments, the growth medium was supplemented with CHIR99021 (Stemgent, 3 μM) and nicotinamide (Sigma-Aldrich, 10 mM) for 4 days before sample collection. For transgene induction in the TetON-YAP-H2B-mCherry aOrgs, DOX (Sigma-

Aldrich, no. D9891, 1μg/ml) was added for 48 hours immediately after splitting.

Replating assays

FEnS and aOrg cultures were passaged using conventional mechanical disruption. Pharmacological inhibitors were added for 24 hours during early or late time points (i.e., 0 to 24 or 72 to 96 hours after passaging). Dimethyl sulfoxide (DMSO) was used as control. At 96 hours, treated organoids were passaged again and kept in control media (ENR without inhibitors). Organoid formation efficiency (relative to DMSO controls) was determined 72 hours after. The same setup was used for the experiment with freshly isolated crypts. The following pharmacological inhibitors were used: MGH-CP1 (Selleckchem, no. S9735, 20 μM), TED-347 (Selleckchem, no. S8951, 20 μM), verteporfin (Sigma-Aldrich, no. SML0534, 0.25 μM), dasatinib (Sigma-Aldrich, no. SML2589, 0.25 to 1 μM), and PF573228 (Tocris, no. 3239, 2.5 to 10 μM).

CAGE sequencing

CAGE libraries for three biological replicates of fetal spheroids and aOrg were prepared as previously described (*14*) with an input of 3000 ng of total RNA. All primers and adapters were purchased from Integrated DNA Technologies. After individually preparing CAGE libraries for each sample, three samples with unique barcodes (CTT, GAT, and ACG) were pooled per sequencing lane, and 30% Phi-X was spiked into each lane. Sequencing was carried out at the National High-throughput DNA Sequencing Centre, University of Copenhagen, with Illumina HiSeq2000.

CAGE data processing

Reads with identical barcodes were matched to their originating samples and, after the removal of barcode sequences, mapped to the mm10 assembly with Bowtie2. Only uniquely mapping reads not mapping to chrM were retained for further analysis. CTSSs (5′ ends of CAGE tags) supported by only a single read were excluded from the analysis. CTSSs were subsequently tags per million (TPM)–normalized (CAGE reads per total mapped reads in library times 10^6). CTSSs on the same strand within 20 base pairs (bp) of each other were merged into tag clusters (TCs) and quantified in all samples (single read CTSSs were included for the quantification). A summit was identified in each TC, defined as the single–base pair position within the TC with the highest total TPM coverage across all samples.

ATAC-seq

ATAC-seq was performed as previously described (*60*) with two biological replicates per condition. Briefly, fetal spheroids and aOrg were released from Matrigel and resuspended in TrypLE Express Enzyme (GIBCO) and incubated at 37°C until a single-cell suspension was obtained. After centrifugation, cells were resuspended in phosphate-buffered saline (PBS) with 1% bovine serum albumin (BSA) and incubated with fluorescent-conjugated primary antibody epithelial cell adhesion molecule (EpCAM)–allophycocyanin (APC) (clone G8.8, eBioscience) diluted 1:500 for 30 min on ice. After washing, 4′,6-diamidino-2-phenylindole (DAPI, Sigma-Aldrich, 1 μM) was added, and 50,000 live ($EpCAM^+$ $DAPI^-$) cells were subsequently sorted on a fluorescence-activated cell sorter (FACS) Aria I (BD Bioscience). Following this, the cells were lysed and, after centrifugation, resuspended in transposase reaction mix and incubated for 30 min at 37°C. After purification, the eluted DNA was polymerase chain reaction (PCR)–amplified with unique barcodes (TAAGGCGA, CGTACTAG, TCCTGAGC, and TAGGCATG) containing PCR primers for multiplexing of samples and purified. The samples were paired-end sequenced with Illumina NextSeq.

ATAC-seq data processing

Paired-end reads were mapped with Bowtie2 against mm10 assembly, and only uniquely mapping reads were retained using samtools. Subsequently, duplicate reads were removed, and regions highly contaminated by duplicate reads (99.9th percentile) as well as ENCODE blacklist regions were masked out. Reads aligning to the plus strand were offset by +4 bp and reads aligning to the minus strand were offset by −5 bp, as described in (*60*). The peaks were called for each replicate using MACS2 without a shifting model and the background lambda as local lambda. Differential accessibility analysis was performed separately for promoters and enhancers using generalized linear model quasi-likelihood framework of edgeR.

Identification of promoters and enhancers and gene-level expression

As we found that only 10% of CAGE signals fell outside of ATAC-seq peaks, only CTSSs overlapping an ATAC-seq peak were retained. Using National Center for Biotechnology Information (NCBI) RefSeq mm10 annotation, we identified peaks overlapping TSSs (±500 bp) or exons (±200 bp) as gene promoters and intronic and intergenic peaks as potential enhancers. For promoters, we retained ATAC peaks overlapping a TC > 0.8 average TPM in all three replicates in at least one condition. For enhancers, a noise cutoff was estimated for the sum of the CAGE TCs overlapping an ATAC peak for all unique ATAC peak lengths. For gene-level expression, the sum of TCs overlapping the gene on the same strand was used. To identify enhancer clusters, we stitched non-exon overlapping transcribed ATAC peaks outside within 12.5 kb from each. Among these clusters, we calculated the pairwise Pearson correlations between all member enhancers, and the clusters with average pairwise correlation >0.5 were defined as internally correlated enhancer clusters.

Exploratory CAGE analysis and differential expression

Principal components analysis was performed for combined TPM-normalized CAGE counts at promoter and enhancers using prcomp function from base R with scaling and centering. Differential expression analysis was performed separately at gene, promoter, and enhancer levels using the generalized linear model quasi-likelihood framework of edgeR. For identifying a set of differentially expressed genes, an absolute $\log_2$ fold change threshold of one was used, *P* values were corrected for multiple testing using Benjamini-Hochberg method, and FDR < 0.05 cutoff was used. For analysis of GO term enrichment, topGO with Fisher′s exact test was used. All expressed genes were used as a background set.

Whole-genome bisulfite sequencing

Genomic DNA of fetal and adult organoids (three biologically independent replicates each) was purified using Genomic DNA Purification Kit (Thermo Fisher Scientific). All six libraries were prepared with ACCEL-NGS METHYL-SEQ DNA Library Kit.

WGBS data processing

After quality trimming with Trim Galore, the reads were mapped, and methylation status was determined with Bismark, in which bisulfite converts the reads in silico before mapping with Bowtie2 to a bisulfite-converted reference genome. We found that the mapping efficiency was low because of the large number of chimeric reads. To mitigate this, the mapping was performed in two steps: First, all reads were mapped in paired-end mode with the option --unmapped, following which, the unmapped R1 was mapped in single-end mode (directional mode) and the unmapped R2 was mapped in single-end mode (--pbat mode). The paired-end and single-end alignments were merged after methylation extraction.

Identification of PMDs and DMRs

Partially methylated domains (PMDs) and non-PMDs were defined using MethylSeekR. A consensus set of PMDs present in all six samples was identified, and FEnS- or saOrg-specific PMDs were defined as regions present in all three replicates from either stage but none of the replicates of the other. We identified DMRs by BSmooth implemented in bsseq. We used the methylation calls processed with Bismark and performed the smoothing and differential methylation analysis with BSmooth. We used only CpGs that were covered by more than four reads in all six samples. The smoothing was done for regions containing at least 70 CpGs or were at least 2-kb wide, whichever is largest, using the whole chromosomes as the smoothing cluster. For computing t-statistics, the variability was estimated on the basis of the fetal samples. For identifying DMRs, we used a cutoff 4.6 based on t-statistic quantiles.

Hi-C

FEnS and aOrg (two biological replicates each) were released from Matrigel and fragmented by repeated washing with cold PBS with 0.1% BSA. The organoid fragments were cross-linked in 2% formaldehyde for 20 min, quenched, and washed. Cells were then lysed, and chromatin was digested with 2 units of DNase I for 5 min. The nuclei were purified with AMPure XP beads and washed, followed by end repair and dA-tailing reactions. Biotin-labeled bridge adapters were then ligated overnight to the fragments followed by another round of purification with AMPure XP beads and washing. The nuclei were treated with T4 Polynucleotide Kinase (PNK) to phosphorylate adapters and ligation before reversal of cross-linking, DNA precipitation, and purification. The ligation products with biotin were then pulled down with MyOne C1 beads followed by washing and end repair, dA-tailing, and ligation of sequencing adapters. The libraries were amplified for 14 PCR cycles with primers containing Nextera barcodes for sample multiplexing: N701 (TCGCCTTA), N702 (CTAGTACG), N703 (TTCTGCCT), and N704 (GCTCAGGA). Libraries were then purified and quantified with Qubit and Fragment Analyzer (Agilent), and the four libraries were pooled and paired-end sequenced with Illumina NextSeq.

Hi-C data processing

Hi-C reads were matched to their originating sample and subsequently qtrimmed with Trim Galore. The reads were mapped and processed with HiC-Pro. We used MAPQ score threshold 30 and excluded read pairs mapping within 1 kb to retain valid pairs and generate ICE-normalized contact maps at 100-kb resolution. All valid read pairs were converted into Juicebox viewable.hic matrixes for visual exploration of interaction patterns with Knight-Ruiz normalization at 500-kb resolution.

Compartment analysis

A/B compartments were identified as previously described (*31*). Briefly, we used Juicer to compute the Pearson′s correlation matrix of the observed/expected interaction matrix of contiguous nonoverlapping 500-kb bins and its first principal component (eigenvector). The signs of eigenvectors were flipped according to gene density, and the bins with positive eigenvalues were assigned to the A compartment and those with negative eigenvalues were assigned to the B compartment. For stringency, we excluded the bins where the eigenvector had an absolute value less than 0.01. We defined compartment-changing regions as bins where the sign of the eigenvector was positive in both replicates of one condition and negative in the other, and the magnitude was larger than 0.01 in all samples.

Correlation of eigenvalues with nuclear lamina interaction values

Hi-C eigenvalues were correlated with the average of previously reported genome-wide DamID lamin interaction values reported as $\log_2$-transformed Dam-fusion/Dam-only ratio of three different murine cell lines: neural precursor cells, astrocytes, and embryonic fibroblasts (*35*).

Differential interaction analysis

For the differential interaction analysis, we used the diffHic package. The Hi-C read pairs were summarized into pairs of contiguous nonoverlapping 100-kb bins, and bin overlapping repeat regions or pairs supported by fewer than 10 read pairs were excluded from further analysis. We used the median abundance of interchromosomal bin pairs to estimate nonspecific ligation rate and required more than fivefold higher abundance than this threshold, combined with a trended filter considering the interaction distance and required higher abundance than a fitted value for that distance, since larger counts are expected for shorter interaction distances. Furthermore, we excluded diagonal interactions within the same bin. After filtering, the data were Locally estimated scatterplot smoothing (LOESS)-normalized, significant differences were found using the generalized linear model quasi-likelihood framework, and the generated *P* values were corrected for multiple testing using the Benjamini-Hochberg method.

Boundary analysis

To identify differential domain boundaries, we used an approach based on directionality index implemented in diffHic (*37*). Briefly, by counting the difference in number of read pairs between the target 100-kb bin and upstream or downstream 1-Mb interval, a directionality index was calculated for each 100-kb bin. After removing low-abundance bins, dispersion estimation, and fitting of generalized linear model, bins where directionality statistic changes between fetal and adult states were identified after multiple testing correction with the Benjamini-Hochberg method. We then identified a set of promoters within 50 kb from a differential boundary and analyzed GO term enrichment using topGO with Fisher′s exact test.

TF binding motif analysis

TF binding analysis was performed separately for enhancers and promoters. Enhancer regions were defined as ±300 bp from enhancer midpoint and promoter regions as −500 to +100 bp around the CAGE summit. Differentially expressed enhancers and promoters in FEnS and aOrg were compared to the background set composed of all expressed enhancers or promoters, respectively. Next, we used the HOMER findMotifsGenome tool to calculate enrichment of previously annotated motifs. HOMER motif logos were extracted from http://homer.ucsd.edu/homer/motif/.

In vivo adult tissue processing for RNA-seq

Crypts were isolated from the proximal 20% of the small intestine and processed to obtain single cells as previously described in three biological replicates (*10*). Briefly, whole epithelium samples were isolated from the proximal 20% of the small intestine using EDTA solution and incubated with collagenase to obtain single-cell suspensions. Following the exclusion of DAPI-negative cells, EpCAM-positive and CD24-mid expressing cells (for adult crypt cells) were purified using an FACSAria III cell sorter. The following primary antibodies were used: EpCAM (Thermo Fisher Scientific, no. 17-5791-82, 1:500), CD45 (BD Biosciences, no. 550994, 1:200), CD31 (BD Biosciences, no. 562861, 1:200), and CD24 (BD Biosciences, no. 553262, 1:200).

RNA sequencing

RNA was collected from three biological replicates using RNAeasy Microkit (Qiagen). For in vivo data, RNA-seq libraries were prepared using the SMARTer Stranded Total RNA-Seq v2 Pico Input Mammalian kit (Takara), as previously described (*10*). Sequencing reads were aligned using the qAlign function from Bioconductor package QuasR with default parameters, assigned to known UCSC genes and quantified with qCount function from QuasR. FEnS and tetON-YAP aOrg datasets were prepared using the TruSeq RNA kit (Illumina) following manufacturer instructions and sequenced with Illumina NextSeq. Mapping and quantification of fastq files were performed via the Rsubread package. Reads were mapped to the mm10 genome assembly using the align function with default settings. Mapped reads were quantified across RefSeq gene models using the featureCounts-function with default settings.

RNA-seq exploratory analysis and differential expression

Differential expression analysis was performed using the generalized linear model quasi-likelihood framework of edgeR. For identifying a set of differentially expressed genes, *P* values were corrected for multiple testing using the Benjamini-Hochberg method and an FDR < 0.05 cutoff was used. Gene set enrichment analyses were performed with the edgeR fry function for a list of YAP-activated genes (*39*), collagen 1–associated signature (*21*), or the gene lists identified through our CAGE and RNA-seq profiling (i.e., FEnS, aOrg, and in vivo E16.5 fetal and adult epithelium; table S5).

Single-cell RNA-seq

FEnS and aOrg grown in ENR medium were dissociated into single cells and FACS-sorted (20,000 live cells per replica) for library preparation with the 10X Genomics v3 Chemistry. cDNA was amplified with 10 PCR cycles, while sample indexing PCR was performed with 11 cycles. Libraries were diluted to 2 nM in elution buffer, and a final amount of 1.7 pM per library was sequenced on an Illumina NextSeq 500 sequencer. For further details on data processing, analyses, and access, see the accompanying manuscript by Hansen *et al.* (*45*).

Immunostainings

Fetal and adult organoids were plated in 96-well imaging plates (Greiner, no. 655090) and fixed in paraformaldehyde (PFA) for 10 min at room temperature (RT). Cells were permeabilized and blocked in PBS–Triton X-100 (TX100) 0.2%, 2% normal goat serum (NGS), 1% BSA, and 100 μM glycine for 1 hour at RT. Primary antibodies were diluted in PBS-TX100 0.2% + BSA 0.5% + NGS 1% and incubated overnight at 4°C with slow agitation. Following washes with 0.1% Tween 20 PBS, the appropriate Alexa Fluor–conjugated secondary antibodies (1:500) were incubated as the primary antibodies. Cells were counterstained with DAPI and phalloidin for 20 min at RT, and RapiClear (Sunjin Lab, no. RC152001) solution was added before imaging. For staining tissue samples, proximal halves of fetal and adult small intestines were collected, embedded in optimal cutting temperature (OCT) compound, and snap-frozen in dry ice. Tissue sections (7 μm thick) were prepared with a microtome and subsequently dried overnight at −80°C plus 20 min at RT. Dried sections were fixed with ice-cold 4% PFA for 10 min. Blocking and permeabilization were performed in PBS containing 0.2% Triton X-100, 2% NGS, 1% BSA, and 100 μM glycine. Primary antibodies were incubated overnight at 4°C in PBS containing 0.2% Triton X-100, 0.5% BSA, and 1% NGS followed by incubation with secondary antibodies in the same buffer for 90 min. All washes were performed with PBS containing 0.1% Tween 20. DAPI was used for nuclei staining. Images were acquired using a laser scanning confocal microscope (Leica Stellaris 8) and analyzed with Fiji. The following primary antibodies were used: YAP (Cell Signaling Technologies, no. 14074, 1:100), SOX17 (R&D Systems, no. AF1924, 1:300), and GATA4 (Santa Cruz Biotechnology, no. sc-25310, 1:500).

Flow cytometry

Organoids were collected in 0.1% BSA solution, spun down, and dissociated into single cells through incubation with TripLE solution at 37° for 5 min. Following centrifugation, cells were resuspended in 1% BSA solution and incubated with anti–SCA1-APC (eBioscience, no. 15-5981-83, 1:1000) or anti–CD117-PECy7 (BD Biosciences, no. 558163, 1:200) for 15 min at RT. DAPI was used as viability staining. Data were collected with LSR Fortessa X20 (BD Bioscience) and analyzed with FlowJo.

Reverse transcription quantitative PCR

Total RNA was extracted using the RNeasy Micro kit (Qiagen) and cDNA-synthesized using random hexamers and Superscript III reverse transcriptase (Invitrogen). Quantitative PCR was performed with PowerUp SYBR Green Master Mix (Thermo Fisher Scientific) in QuantStudio 7 Flex Real-Time PCR System (Applied Biosciences). Relative expression values were calculated using the ΔΔCt method. Average Ct values for glyceraldehyde-3-phosphate dehydrogenase (*Gapdh*) and *Tubb5* were used for normalization. Primer sequences are provided in table S6.

Western blotting

Samples were lysed in radioimmunoprecipitation assay buffer [50 mM tris-HCl (pH 8.0), 150 mM NaCl, 0.1% SDS, 0.15% Na-

Deoxycholate, 1% NP-40, and 2 mM EDTA (pH 8.0)] containing cOmplete protease inhibitors (Roche, no. 11697498001). Protein content was quantified by standard bicinchoninic acid (BCA) assay using the Pierce BCA Protein Assay Kit (Thermo Fisher Scientific, no. 23227). Equal protein amounts (10 μg/sample) were run on gradient 4 to 12% bis-tris protein gels (Thermo Fisher Scientific, no. NP0329BOX) and transferred to nitrocellulose membranes (Sigma-Aldrich, no. GE10600016). Membranes were blocked in 5% milk solution for 2 hours at RT and probed overnight at 4°C with primary antibodies directed against fibronectin (Sigma-Aldrich, F3648), collagen IV (Abcam, no. ab6586), and GAPDH (Millipore, no. mab374) in 1:1000 dilution. After three washes in 1× Tris-buffered saline with 0.1% Tween® 20 detergent (TBST) buffer (10 min each), membranes were incubated with peroxidase-labeled anti-rabbit (Cytiva, no. NA934V5) or anti-mouse (Abcam, no. ab205719) secondary antibody (1:10,000) for an hour at RT. After subsequent washes in 1× TBST buffer, enhanced chemiluminescence substrate kit (Thermo Fisher Scientific, no. 32132) was used for band detection according to the manufacturer's instructions. Membranes were imaged on the ChemiDoc MP imaging system (Bio-Rad Laboratories Inc.).

Supplementary Materials

This PDF file includes:
Figs. S1 to S6
Legends for tables S1 to S6

Other Supplementary Material for this manuscript includes the following:
Tables S1 to S6

REFERENCES AND NOTES

1. J. Guiu, K. B. Jensen, From definitive endoderm to gut-a process of growth and maturation. *Stem Cells Dev.* **24**, 1972–1983 (2015).
2. A. M. Chin, D. R. Hill, M. Aurora, J. R. Spence, Morphogenesis and maturation of the embryonic and postnatal intestine. *Semin. Cell Dev. Biol.* **66**, 81–93 (2017).
3. N. Barker, J. H. van Es, J. Kuipers, P. Kujala, M. van den Born, M. Cozijnsen, A. Haegebarth, J. Korving, H. Begthel, P. J. Peters, H. Clevers, Identification of stem cells in small intestine and colon by marker gene Lgr5. *Nature* **449**, 1003–1007 (2007).
4. J. Guiu, E. Hannezo, S. Yui, S. Demharter, S. Ulyanchenko, M. Maimets, A. Jørgensen, S. Perlman, L. Lundvall, L. S. Mamsen, A. Larsen, R. H. Olesen, C. Y. Andersen, L. L. Thuesen, K. J. Hare, T. H. Pers, K. Khodosevich, B. D. Simons, K. B. Jensen, Tracing the origin of adult intestinal stem cells. *Nature* **570**, 107–111 (2019).
5. H. Gehart, H. Clevers, Tales from the crypt: New insights into intestinal stem cells. *Nat. Rev. Gastroenterol. Hepatol.* **16**, 19–34 (2019).
6. M. Bjerknes, H. Cheng, The stem-cell zone of the small intestinal epithelium. II. Evidence from paneth cells in the newborn mouse. *Am. J. Anat.* **160**, 65–75 (1981).
7. B.-M. Kim, J. Mao, M. M. Taketo, R. A. Shivdasani, Phases of canonical Wnt signaling during the development of mouse intestinal epithelium. *Gastroenterology* **133**, 529–538 (2007).
8. A. E. Shyer, T. R. Huycke, C. Lee, L. Mahadevan, C. J. Tabin, Bending gradients: How the intestinal stem cell gets its home. *Cell* **161**, 569–580 (2015).
9. K. D. Sumigray, M. Terwilliger, T. Lechler, Morphogenesis and compartmentalization of the intestinal crypt. *Dev. Cell* **45**, 183–197.e5 (2018).
10. M. Maimets, M. T. Pedersen, J. Guiu, J. Dreier, M. Thodberg, Y. Antoku, P. J. Schweiger, L. Rib, R. B. Bressan, Y. Miao, K. C. Garcia, A. Sandelin, P. Serup, K. B. Jensen, Mesenchymal-epithelial crosstalk shapes intestinal regionalisation via Wnt and Shh signalling. *Nat. Commun.* **13**, 715 (2022).
11. T. Sato, R. G. Vries, H. J. Snippert, M. van de Wetering, N. Barker, D. E. Stange, J. H. van Es, A. Abo, P. Kujala, P. J. Peters, H. Clevers, Single Lgr5 stem cells build crypt-villus structures in vitro without a mesenchymal niche. *Nature* **459**, 262–265 (2009).
12. R. P. Fordham, S. Yui, N. R. Hannan, C. Soendergaard, A. Madgwick, P. J. Schweiger, O. H. Nielsen, L. Vallier, R. A. Pedersen, T. Nakamura, M. Watanebe, K. B. Jensen, Transplantation of expanded fetal intestinal progenitors contributes to colon regeneration after injury. *Cell Stem Cell* **13**, 734–744 (2013).
13. R. C. Mustata, G. Vasile, V. Fernandez-Vallone, S. Strollo, A. Lefort, F. Libert, D. Monteyne, D. Pérez-Morga, G. Vassart, M.-I. Garcia, Identification of *Lgr5*-independent spheroid-generating progenitors of the mouse fetal intestinal epithelium. *Cell Rep.* **5**, 421–432 (2013).
14. H. Takahashi, T. Lassmann, M. Murata, P. Carninci, 5′ end-centered expression profiling using cap-analysis gene expression and next-generation sequencing. *Nat. Protoc.* **7**, 542–561 (2012).
15. L. G. van der Flier, M. E. van Gijn, P. Hatzis, P. Kujala, A. Haegebarth, D. E. Stange, H. Begthel, M. van den Born, V. Guryev, I. Oving, J. H. van Es, N. Barker, P. J. Peters, M. van de Wetering, H. Clevers, Transcription factor achaete scute-like 2 controls intestinal stem cell fate. *Cell* **136**, 903–912 (2009).
16. S. R. Finkbeiner, D. R. Hill, C. H. Altheim, P. H. Dedhia, M. J. Taylor, Y. H. Tsai, A. M. Chin, M. M. Mahe, C. L. Watson, J. J. Freeman, R. Nattiv, M. Thomson, O. D. Klein, N. F. Shroyer, M. A. Helmrath, D. H. Teitelbaum, P. J. Dempsey, J. R. Spence, Transcriptome-wide analysis reveals hallmarks of human intestine development and maturation in vitro and in vivo. *Stem Cell Rep.* **4**, 1140–1155 (2015).
17. N. Takeda, R. Jain, M. R. LeBoeuf, Q. Wang, M. M. Lu, J. A. Epstein, Interconversion between intestinal stem cell populations in distinct niches. *Science* **334**, 1420–1424 (2011).
18. J. Muñoz, D. E. Stange, A. G. Schepers, M. van de Wetering, B. K. Koo, S. Itzkovitz, R. Volckmann, K. S. Kung, J. Koster, S. Radulescu, K. Myant, R. Versteeg, O. J. Sansom, J. H. van Es, N. Barker, A. van Oudenaarden, S. Mohammed, A. J. Heck, H. Clevers, The Lgr5 intestinal stem cell signature: Robust expression of proposed quiescent '+4' cell markers. *EMBO J.* **3**, 3079–3091 (2012).
19. A. K. San Roman, B. E. Aronson, S. D. Krasinski, R. A. Shivdasani, M. P. Verzi, Transcription factors GATA4 and HNF4A control distinct aspects of intestinal homeostasis in conjunction with transcription factor CDX2. *J. Biol. Chem.* **290**, 1850–1860 (2015).
20. M. P. Verzi, H. Shin, H. H. He, R. Sulahian, C. A. Meyer, R. K. Montgomery, J. C. Fleet, M. Brown, X. S. Liu, R. A. Shivdasani, Differentiation-specific histone modifications reveal dynamic chromatin interactions and partners for the intestinal transcription factor CDX2. *Dev. Cell* **19**, 713–726 (2010).
21. S. Yui, L. Azzolin, M. Maimets, M. T. Pedersen, R. P. Fordham, S. L. Hansen, H. L. Larsen, J. Guiu, M. R. P. Alves, C. F. Rundsten, J. V. Johansen, Y. Li, C. D. Madsen, T. Nakamura, M. Watanabe, O. H. Nielsen, P. J. Schweiger, S. Piccolo, K. B. Jensen, YAP/TAZ-dependent reprogramming of colonic epithelium links ECM remodeling to tissue regeneration. *Cell Stem Cell* **22**, 35–49.e7 (2018).
22. M. Kanai-Azuma, Y. Kanai, J. M. Gad, Y. Tajima, C. Taya, M. Kurohmaru, Y. Sanai, H. Yonekawa, K. Yazaki, P. P. L. Tam, Y. Hayashi, Depletion of definitive gut endoderm in *Sox17*-null mutant mice. *Development* **129**, 2367–2379 (2002).
23. R. Andersson, P. R. Andersen, E. Valen, L. J. Core, J. Bornholdt, M. Boyd, T. H. Jensen, A. Sandelin, Nuclear stability and transcriptional directionality separate functionally distinct RNA species. *Nat. Commun.* **5**, 5336 (2014).
24. R. Andersson, C. Gebhard, I. Miguel-Escalada, I. Hoof, J. Bornholdt, M. Boyd, Y. Chen, X. Zhao, C. Schmidl, T. Suzuki, E. Ntini, E. Arner, E. Valen, L. Li, L. Schwarzfischer, D. Glatz, J. Raithel, B. Lilje, N. Rapin, F. O. Bagger, M. Jørgensen, P. R. Andersen, N. Bertin, O. Rackham, A. M. Burroughs, J. K. Baillie, Y. Ishizu, Y. Shimizu, E. Furuhata, S. Maeda, Y. Negishi, C. J. Mungall, T. F. Meehan, T. Lassmann, M. Itoh, H. Kawaji, N. Kondo, J. Kawai, A. Lennartsson, C. O. Daub, P. Heutink, D. A. Hume, T. H. Jensen, H. Suzuki, Y. Hayashizaki, F. Müller, A. R. R. Forrest, P. Carninci, M. Rehli, A. Sandelin, An atlas of active enhancers across human cell types and tissues. *Nature* **507**, 455–461 (2014).
25. D. Hnisz, B. J. Abraham, T. I. Lee, A. Lau, V. Saint-André, A. A. Sigova, H. A. Hoke, R. A. Young, Super-enhancers in the control of cell identity and disease. *Cell* **155**, 934–947 (2013).
26. W. A. Whyte, D. A. Orlando, D. Hnisz, B. J. Abraham, C. Y. Lin, M. H. Kagey, P. B. Rahl, T. I. Lee, R. A. Young, Master transcription factors and mediator establish super-enhancers at key cell identity genes. *Cell* **153**, 307–319 (2013).
27. S. F. Schmidt, B. D. Larsen, A. Loft, R. Nielsen, J. G. Madsen, S. Mandrup, Acute TNF-induced repression of cell identity genes is mediated by NFκB-directed redistribution of cofactors from super-enhancers. *Genome Res.* **25**, 1281–1294 (2015).
28. R. Fenouil, P. Cauchy, F. Koch, N. Descostes, J. Z. Cabeza, C. Innocenti, P. Ferrier, S. Spicuglia, M. Gut, I. Gut, J.-C. Andrau, CpG islands and GC content dictate nucleosome depletion in a transcription-independent manner at mammalian promoters. *Genome Res.* **12**, 2399–2408 (2012).
29. S. Saxonov, P. Berg, D. L. Brutlag, A genome-wide analysis of CpG dinucleotides in the human genome distinguishes two distinct classes of promoters. *Proc. Natl. Acad. Sci. U.S.A.* **103**, 1412–1417 (2006).
30. J. Kazakevych, S. Sayols, B. Messner, C. Krienke, N. Soshnikova, Dynamic changes in chromatin states during specification and differentiation of adult intestinal stem cells. *Nucleic Acids Res.* **45**, 5770–5784 (2017).
31. E. Lieberman-Aiden, N. L. van Berkum, L. Williams, M. Imakaev, T. Ragoczy, A. Telling, I. Amit, B. R. Lajoie, P. J. Sabo, M. O. Dorschner, R. Sandstrom, B. Bernstein, M. A. Bender, M. Groudine, A. Gnirke, J. Stamatoyannopoulos, L. A. Mirny, E. S. Lander, J. Dekker,

Comprehensive mapping of long-range interactions reveals folding principles of the human genome. *Science* **326**, 289–293 (2009).
32. J. R. Dixon, I. Jung, S. Selvaraj, Y. Shen, J. E. Antosiewicz-Bourget, A. Y. Lee, Z. Ye, A. Kim, N. Rajagopal, W. Xie, Y. Diao, J. Liang, H. Zhao, V. V. Lobanenkov, J. R. Ecker, J. A. Thomson, B. Ren, Chromatin architecture reorganization during stem cell differentiation. *Nature* **518**, 331–336 (2015).
33. R. Stadhouders, G. J. Filion, T. Graf, Transcription factors and 3D genome conformation in cell-fate decisions. *Nature* **569**, 345–354 (2019).
34. S. E. Johnstone, A. Reyes, Y. Qi, C. Adriaens, E. Hegazi, K. Pelka, J. H. Chen, L. S. Zou, Y. Drier, V. Hecht, N. Shoresh, M. K. Selig, C. A. Lareau, S. Iyer, S. C. Nguyen, E. F. Joyce, N. Hacohen, R. A. Irizarry, B. Zhang, M. J. Aryee, B. E. Bernstein, Large-scale topological changes restrain malignant progression in colorectal cancer. *Cell* **182**, 1474–1489.e23 (2020).
35. W. Meuleman, D. Peric-Hupkes, J. Kind, J.-B. Beaudry, L. Pagie, M. Kellis, M. Reinders, L. Wessels, B. van Steensel, Constitutive nuclear lamina-genome interactions are highly conserved and associated with A/T-rich sequence. *Genome Res.* **23**, 270–280 (2013).
36. J. P. Fortin, K. D. Hansen, Reconstructing A/B compartments as revealed by Hi-C using long-range correlations in epigenetic data. *Genome Biol.* **16**, 180 (2015).
37. J. R. Dixon, S. Selvaraj, F. Yue, A. Kim, Y. Li, Y. Shen, M. Hu, J. S. Liu, B. Ren, Topological domains in mammalian genomes identified by analysis of chromatin interactions. *Nature* **485**, 376–380 (2012).
38. A. Totaro, T. Panciera, S. Piccolo, YAP/TAZ upstream signals and downstream responses. *Nat. Cell Biol.* **20**, 888–899 (2018).
39. A. Gregorieff, Y. Liu, M. R. Inanlou, Y. Khomchuk, J. L. Wrana, Yap-dependent reprogramming of Lgr5$^+$ stem cells drives intestinal regeneration and cancer. *Nature* **526**, 715–718 (2015).
40. Y. Liu-Chittenden, B. Huang, J. S. Shim, Q. Chen, S.-J. Lee, R. A. Anders, J. O. Liu, D. Pan, Genetic and pharmacological disruption of the TEAD-YAP complex suppresses the oncogenic activity of YAP. *Genes Dev.* **26**, 1300–1305 (2012).
41. K. Bum-Erdene, D. Zhou, G. Gonzalez-Gutierrez, M. K. Ghozayel, Y. Si, D. Xu, H. E. Shannon, B. J. Bailey, T. W. Corson, K. E. Pollok, C. D. Wells, S. O. Meroueh, Small-molecule covalent modification of conserved cysteine leads to allosteric inhibition of the TEAD·Yap protein-protein interaction. *Cell Chem. Biol.* **26**, 378–389.e13 (2019).
42. Q. Li, Y. Sun, G. K. Jarugumilli, S. Liu, K. Dang, J. L. Cotton, J. Xiol, P. Y. Chan, M. DeRan, L. Ma, R. Li, L. J. Zhu, J. H. Li, A. B. Leiter, Y. T. Ip, F. D. Camargo, X. Luo, R. L. Johnson, X. Wu, J. Mao, Lats1/2 sustain intestinal stem cells and Wnt activation through TEAD-dependent and independent transcription. *Cell Stem Cell* **26**, 675–692.e8 (2020).
43. L. Azzolin, T. Panciera, S. Soligo, E. Enzo, S. Bicciato, S. Dupont, S. Bresolin, C. Frasson, G. Basso, V. Guzzardo, A. Fassina, M. Cordenonsi, S. Piccolo, YAP/TAZ incorporation in the β-Catenin destruction complex orchestrates the Wnt response. *Cell* **158**, 157–170 (2014).
44. D. Serra, U. Mayr, A. Boni, I. Lukonin, M. Rempfler, L. Challet-Meylan, M. B. Stadler, P. Strnad, P. Papasaikas, D. Vischi, A. Waldt, G. Roma, P. Liberali, Self-organization and symmetry breaking in intestinal organoid development. *Nature* **569**, 66–72 (2019).
45. S. L. Hansen, H. L. Larsen, L. M. Pikkupeura, G. Maciag, J. Guiu, I. Müller, D. Clement, C. Mueller, J. V. Johansen, K. Helin, M. Lerdrup, K. B. Jensen, An organoid-based CRISPR/Cas9 screen for regulators of intestinal epithelial maturation. *Sci. Adv.*
46. K. K. Banerjee, M. Saxena, N. Kumar, L. Chen, A. Cavazza, N. H. Toke, N. K. O'Neill, S. Madha, U. Jadhav, M. P. Verzi, R. A. Shivdasani, Enhancer, transcriptional, and cell fate plasticity precedes intestinal determination during endoderm development. *Genes Dev.* **32**, 1430–1442 (2018).
47. L. Chen, N. H. Toke, S. Luo, R. P. Vasoya, R. Aita, A. Parthasarathy, Y.-H. Tsai, J. R. Spence, M. P. Verzi, HNF4 factors control chromatin accessibility and are redundantly required for maturation of the fetal intestine. *Development* **146**, dev179432 (2019).
48. M. Srivillibhuthur, B. N. Warder, N. H. Toke, P. P. Shah, Q. Feng, N. Gao, E. M. Bonder, M. P. Verzi, TFAM is required for maturation of the fetal and adult intestinal epithelium. *Dev. Biol.* **439**, 92–101 (2018).
49. U. Jadhav, A. Cavazza, K. K. Banerjee, H. Xie, N. K. O'Neill, V. Saenz-Vash, Z. Herbert, S. Madha, S. H. Orkin, H. Zhai, R. A. Shivdasani, Extensive recovery of embryonic enhancer and gene memory stored in hypomethylated enhancer DNA. *Mol. Cell* **74**, 542–554.e5 (2019).
50. Y. Zheng, D. Pan, The hippo signaling pathway in development and disease. *Dev. Cell* **50**, 264–282 (2019).
51. D. E. Cohen, D. Melton, Turning straw into gold: Directing cell fate for regenerative medicine. *Nat. Rev. Genet.* **12**, 243–252 (2011).
52. A. Trounson, N. D. Dewitt, Stem cell biology: Towards the reality of cell therapeutics. *Nat. Cell Biol.* **14**, 331 (2012).
53. E. G. Vasquez, N. Nasreddin, G. N. Valbuena, E. J. Mulholland, H. L. Belnoue-Davis, H. R. Eggington, R. O. Schenck, V. M. Wouters, P. Wirapati, K. Gilroy, T. R. M. Lannagan, D. J. Flanagan, A. K. Najumudeen, S. Omwenga, A. M. B. McCorry, A. Easton, V. H. Koelzer, J. E. East, D. Morton, L. Trusolino, T. Maughan, A. D. Campbell, M. B. Loughrey, P. D. Dunne, P. Tsantoulis, D. J. Huels, S. Tejpar, O. J. Sansom, S. J. Leedham, Dynamic and adaptive cancer stem cell population admixture in colorectal neoplasia. *Cell Stem Cell* **29**, 1213–1228.e8 (2022).
54. P. Bala, J. P. Rennhack, D. Aitymbayev, C. Morris, S. M. Moyer, G. N. Duronio, P. Doan, Z. Li, X. Liang, J. L. Hornick, M. B. Yurgelun, W. C. Hahn, N. S. Sethi, Aberrant cell state plasticity mediated by developmental reprogramming precedes colorectal cancer initiation. *Sci. Adv.* **9**, eadf0927 (2023).
55. A. Ayyaz, S. Kumar, B. Sangiorgi, B. Ghoshal, J. Gosio, S. Ouladan, M. Fink, S. Barutcu, D. Trcka, J. Shen, K. Chan, J. L. Wrana, A. Gregorieff, Single-cell transcriptomes of the regenerating intestine reveal a revival stem cell. *Nature* **569**, 121–125 (2019).
56. M. Martín-Alonso, S. Iqbal, P. M. Vornewald, H. T. Lindholm, M. J. Damen, F. Martínez, S. Hoel, A. Díez-Sánchez, M. Altelaar, P. Katajisto, A. G. Arroyo, M. J. Oudhoff, Smooth muscle-specific MMP17 (MT4-MMP) regulates the intestinal stem cell niche and regeneration after damage. *Nat. Commun.* **12**, 6741 (2021).
57. P. J. Schweiger, M. Le Bouteiller, S. Yui, M. Thodberg, D. Clement, K. B. Jensen, Extracellular matrix interactions provide tumor cells with an escape mechanism for commitment to differentiation. *Gastroenterology* **163**, 1688–1690.e3 (2022).
58. M. A. J. Koppens, H. Davis, G. N. Valbuena, E. J. Mulholland, N. Nasreddin, M. Colombe, A. Antanaviciute, S. Biswas, M. Friedrich, L. Lee; Oxford IBD Cohort Investigators, L. M. Wang, V. H. Koelzer, J. E. East, A. Simmons, D. J. Winton, S. J. Leedham, Bone morphogenetic protein pathway antagonism by Grem1 regulates epithelial cell fate in intestinal regeneration. *Gastroenterology* **161**, 239–254.e9 (2021).
59. L. Jansson, J. Larsson, Normal hematopoietic stem cell function in mice with enforced expression of the Hippo signaling effector YAP1. *PLOS ONE* **7**, e32013 (2012).
60. J. D. Buenrostro, P. G. Giresi, L. C. Zaba, H. Y. Chang, W. J. Greenleaf, Transposition of native chromatin for fast and sensitive epigenomic profiling of open chromatin, DNA-binding proteins and nucleosome position. *Nat. Methods* **10**, 1213–1218 (2013).

Acknowledgments: We thank J. Larsson, University of Lund, for the inducible YAP1 mouse model, G. Dela Cruz for assistance with flow cytometry, and members of the K.B.J. and A.S. laboratories for technical assistance and comments on the manuscript. **Funding:** Individual authors were supported by postdoctoral fellowships Lundbeck Foundation (L.M.P. and H.L.L.: R303-2018-3391; D.M.: R347-2020-2304), EMBO (R.B.B.: ALT946-2019), Rubicon (K.L.: 019.211EN.007), and Marie Skłodowska-Curie programs (R.B.B.: 895802/H2020-MSCA-IF-2019; J.G.: 656099/H2020-MSCA-IF-2014). Work in the K.B.J. laboratory was supported by the Novo Nordisk Foundation (NNF20OC0064376), the Danish Cancer Society (R124-A7724), the Danish Medical Research Council (8020-00085B and 0134-00111B), and European Union's Horizon 2020 research and innovation program (grant agreement STEMHEALTH ERCCoG682665). Work in the A.S. laboratory was supported by ERC under European Union's Horizon 2020 research and innovation program (MSCA ITN pHioniC), Lundbeck Foundation, Danish Cancer Society, Danish Council for Independent Research, Innovation Fund Denmark, and the Novo Nordisk Foundation. The Novo Nordisk Foundation Center for Stem Cell Medicine is supported by Novo Nordisk Foundation grants (NNF21CC0073729). **Author contributions:** Conceptualization: L.M.P., R.B.B., J.G., A.S., and K.B.J. Methodology: L.M.P., R.B.B., J.G., Y.C., V.B. A.S., and K.B.J. Investigation: L.M.P., R.B.B., J.G., M.M., P.J.S., S.L.H., H.L.L., K.L., and J.B. Formal analysis: L.M.P., R.B.B., Y.C., D.M., and G.J.M. Resources: M.M., M.T.P., J.M.Y.T and S.L.H. Writing—original draft: L.M.P. and R.B.B. Writing—review and editing: L.M.P., R.B.B., A.S., and K.B.J. Supervision: A.S. and K.B.J. Funding acquisition: A.S. and K.B.J. **Competing interests:** The authors declare that they have no competing interests. **Data and materials availability:** All raw and processed sequencing data generated in this study have been submitted to the NCBI Gene Expression Omnibus (GEO; https://ncbi.nlm.nih.gov/geo/) under accession numbers GSE228519. In vivo fetal data are available under accession number GSE183671. To facilitate the access to the community, we generated a user-friendly webpage that allows visualization of differentially expressed promoters and enhancers, as well as DNA methylation and chromatin structure patterns. The page can be accessed through the link: https://shiny.binf.ku.dk/fetal_adult_regulatory_app/. Requests for the YAP1 inducible mouse model should be sent to J. Larsson, University of Lund. All data needed to evaluate the conclusions in the paper are present in the paper and/or the Supplementary Materials.

Submitted 22 November 2022
Accepted 8 June 2023
Published 12 July 2023
10.1126/sciadv.adf9460

ScienceAdvances

Transcriptional and epigenomic profiling identifies YAP signaling as a key regulator of intestinal epithelium maturation

Laura M. Pikkupeura, Raul B. Bressan, Jordi Guiu, Yun Chen, Martti Maimets, Daniela Mayer, Pawel J. Schweiger, Stine L. Hansen, Grzegorz J. Maciag, Hjalte L. Larsen, Kadi Lhmussaar, Marianne Terndrup Pedersen, Joji M.Yap Teves, Jette Bornholdt, Vladimir Benes, Albin Sandelin, and Kim B. Jensen

Sci. Adv., **9** (28), eadf9460.
DOI: 10.1126/sciadv.adf9460

Science Advances (ISSN) is published by the American Association for the Advancement of Science. 1200 New York Avenue NW, Washington, DC 20005. The title *Science Advances* is a registered trademark of AAAS.